



Title	Spatial and Temporal Growth of Perturbations in Open-Channel Viscous Transverse Shear Flow
Author(s)	de Lima, Adriano C.; Izumi, Norihiro
Citation	Journal of hydraulic engineering, 142(12), 04016067 <a href="https://doi.org/10.1061/(ASCE)HY.1943-7900.0001220">https://doi.org/10.1061/(ASCE)HY.1943-7900.0001220</a>
Issue Date	2016-12
Doc URL	<a href="http://hdl.handle.net/2115/64032">http://hdl.handle.net/2115/64032</a>
Type	article (author version)
Note(URL)	<a href="http://ascelibrary.org/doi/10.1061/%28ASCE%29HY.1943-7900.0001220">http://ascelibrary.org/doi/10.1061/%28ASCE%29HY.1943-7900.0001220</a>
File Information	ascexmpl.pdf



[Instructions for use](#)

# SPATIAL AND TEMPORAL GROWTH OF PERTURBATIONS IN OPEN-CHANNEL VISCOUS TRANSVERSE SHEAR FLOW

Adriano C. de Lima<sup>1</sup>, Norihiro Izumi<sup>2</sup>

## ABSTRACT

The comparison between spatial and temporal growth of perturbations in a shear layer is revisited for the case of a viscous open-channel flow with velocity inflection. Turbulence is characterized by two distinct scales: a sub-depth turbulence associated with the bed shear stress and a large-scale turbulence associated with the large horizontal eddies which develop in the shear layer. Temporal and spatial linear stability analyses are performed. The base flow is assumed to be affected only by the sub-depth scale turbulence. Therefore, the base flow represents not the average flow but the flow completely free of the effect of the instability of the shear layer. Temporal and spatial approaches present less discrepancy in the viscous than in the previously analyzed inviscid case. In particular, the phase velocity was found to be strongly correlated to the frequency in both the temporal and spatial approaches.

**Keywords:** Spatial and temporal linear stability analysis, open-channel viscous flow, shear layer instability, kinematic eddy viscosity.

## INTRODUCTION

Geophysical flows with velocity inflection and transverse shear are observed, for example, in composite channels, in inflows at channel junctions, in channels where the bottom roughness varies laterally, or in channels with lateral vegetation or pile dikes (Tamai et al. 1986; Chu et al. 1991; Ikeda et al. 1991; Ikeda et al. 1994; Tsujimoto and Kitamura 1995; Nadaoka and Yagi 1998; Uijtewaal and Booij 2000; Su and Li 2002; Prooijen and Uijtewaal 2002; White and Nepf 2007).

---

<sup>1</sup>Division of Field Engineering for the Environment, Graduate School of Engineering, Hokkaido University, Sapporo, Japan, 0608628. E-mail: adriano@eng.hokudai.ac.jp.

<sup>2</sup>Division of Field Engineering for the Environment, Graduate School of Engineering, Hokkaido University, Sapporo, Japan, 0608628. E-mail: nizumi@eng.hokudai.ac.jp.

23 Transverse shear results in a Kelvin-Helmholtz instability with large-scale horizontal vortices cen-  
24 tered around the velocity inflection point (Ikeda et al. 1994; Prooijen and Uijttewaai 2002; White  
25 and Nepf 2007). These vortices have a strong influence on the velocity distribution and the amount  
26 of discharge conveyed by a channel without overflow, and enhance the lateral mixing of not only  
27 the flow itself, but also the substances transported by the flow. Precise estimations of discharge ca-  
28 pacity, velocity distribution and shear distribution in channels and rivers are required for practical  
29 engineering problems such as river restoration, flood reduction measures, flood plain management,  
30 control of sediment and pollutant transport in rivers, and aquatic habitat evaluation (Uijttewaai and  
31 Booij 2000; Kolyshkin and Ghidaoui 2002; Carnie et al. 2015).

32 Stability characteristics of transverse shear layers have been studied extensively by means  
33 of linear stability analysis. The inviscid flow assumption was employed in the early works of  
34 Michalke (1964, 1965) and then by e.g. Monkewitz and Huerre (1982), Tamai et al. (1986), Chu  
35 et al. (1991), Ikeda et al. (1994) and White and Nepf (2007). Under the inviscid flow assumption,  
36 the perturbation equations in these studies are reduced to modified Rayleigh equations. On the  
37 other hand, the formulations with turbulence viscosity, such as those of Prooijen and Uijttewaai  
38 (2002), Ghidaoui and Kolyshkin (1999), Kolyshkin and Ghidaoui (2002), Chen and Jirka (1997)  
39 and Lima and Izumi (2014a, 2014b), lead to modified Orr-Sommerfeld equations. The inviscid  
40 flow assumption is a reasonable simplification for flows at large Reynolds numbers or flows where  
41 the changes in the depth, bottom roughness or vegetation density across the channel are gradual.

42 In most of the previous works mentioned above a stability analysis was performed for the  
43 temporal case, in which the disturbance is formulated as timely-growing, with the exception of  
44 Michalke (1965), Monkewitz and Huerre (1982) and White and Nepf (2007), who performed the  
45 analysis for the spatial case of an inviscid flow. It is widely acknowledged that the results of the  
46 spatial stability analysis tend to be in better agreement with experimental data than those from  
47 the temporal stability analysis. However, the spatial stability analysis of viscous flows leads to  
48 a nonlinear eigenvalue problem which is more complicated to solve than the linear eigenvalue  
49 problem resulting from the temporal approach.

50 In the present work, spatial and temporal linear stability analyses are performed for the case  
51 of a viscous shear layer in an open-channel flow. The flow is formulated with the use of the St.  
52 Venant shallow water equations with the Reynolds stress expressed by a kinematic eddy viscosity  
53 representing turbulence with a length scale smaller than the flow depth (Lima and Izumi 2014a).  
54 This is different from previous formulations with turbulence viscosity (Prooijen and Uijttewaal  
55 2002; Ghidaoui and Kolylshkin 1999) where the Reynolds stress is modeled employing a kinematic  
56 eddy viscosity which is affected by the lateral motions due to the shear layer.

57 Results from the spatial and temporal analysis are compared, and the differences among both  
58 approaches are found to be less relevant than those from Michalke (1965). The perturbed veloc-  
59 ity cross-distribution and the phase and group velocities determined for the temporal case in the  
60 present work are particularly distinct from those from Michalke (1965).

## 61 **CONCEPTUAL MODEL AND ANALYTICAL FORMULATION**

62 The formulation employed in the present work follows that of Lima and Izumi (2014a, 2014b),  
63 who performed stability analyses for the temporal case. The application of this formulation to the  
64 growth of disturbances in space is novel. A wide rectangular open-channel flow with an inflection  
65 point in the depth-averaged streamwise velocity is considered. It is assumed that the velocity  
66 gradient is due to the presence of lateral emergent rigid vegetation (pile dikes), as depicted in  
67 Fig. 1. The vegetation is modeled by an array of regularly spaced cylinders with a uniform diameter  
68 installed only on one side of the channel, a set up which has been widely used in previous works  
69 (e.g., Ikeda et al. (1991), Tsujimoto (1991), Ikeda et al. (1994), Kitamura et al. (1998), Su and  
70 Li (2002), White and Nepf (2007, 2008)). The streamwise coordinate is denoted by  $\tilde{x}$  and the  
71 transverse coordinate is denoted by  $\tilde{y}$ , the origin of which being taken at the interface between  
72 the non-vegetated and vegetated zones, assuming positive values in the former. The widths of the  
73 non-vegetated and vegetated zones are denoted by  $\tilde{B}$  and  $\tilde{B}_v$ , respectively. The channel bottom  
74 has a constant slope along its streamwise direction denoted by  $S$ . The rigid-lid assumption is not  
75 employed.

76 The horizontal length scale of the vortices is commonly large compared with the scale of the

77 flow depth. The generation of such thin vortices can be described by the depth-averaged shallow  
 78 water formulation. The momentum and the continuity equations are then introduced in the form

$$79 \quad \frac{\partial \overline{\tilde{U}}}{\partial \tilde{t}} + \left( \overline{\tilde{U}} \cdot \tilde{\nabla} \right) \overline{\tilde{U}} = \tilde{g} - \tilde{g} \tilde{\nabla} \overline{\tilde{H}} - \frac{\overline{\tilde{T}_b} + \overline{\tilde{D}}}{\tilde{\rho} \overline{\tilde{H}}} + \tilde{\nu}_T \tilde{\nabla}^2 \overline{\tilde{U}}, \quad (1a)$$

$$80 \quad \frac{\partial \overline{\tilde{H}}}{\partial \tilde{t}} + \tilde{\nabla} \cdot \left( \overline{\tilde{H} \tilde{U}} \right) = 0, \quad (1b)$$

81 where  $\tilde{t}$  is time,  $\tilde{U} = (\tilde{U}, \tilde{V})$  is the velocity vector with components  $\tilde{U}$  and  $\tilde{V}$  at the  $\tilde{x}$  and  $\tilde{y}$   
 82 directions, respectively,  $\tilde{T}_b$  is the bed shear stress vector,  $\tilde{D}$  is the vegetation drag stress vector,  
 83  $\tilde{g} = (\tilde{g}S, 0)$  is the gravity vector, where  $\tilde{g}$  is the gravity acceleration and  $S$  is the bed slope,  $\tilde{H}$   
 84 is the flow depth,  $\tilde{\rho}$  is the density of the fluid,  $\tilde{\nu}_T$  is the kinematic eddy viscosity,  $\tilde{\nabla} = \left( \frac{\partial}{\partial \tilde{x}}, \frac{\partial}{\partial \tilde{y}} \right)$   
 85 and  $\tilde{\nabla}^2 = \tilde{\nabla} \cdot \tilde{\nabla}$ . The tilde denotes dimensional variables and the overline denotes variables  
 86 averaged over a short time scale corresponding with the sub-depth scale turbulences. The overline  
 87 is dropped afterwards for simplicity.

88 The bed shear stress is related to the flow velocity by means of the bed friction coefficient  $C_f$ ,  
 89 such that

$$90 \quad \tilde{T}_b = (\tilde{T}_{bx}, \tilde{T}_{by}) = \tilde{\rho} C_f (\tilde{U}^2 + \tilde{V}^2)^{1/2} (\tilde{U}, \tilde{V}), \quad (2)$$

91 where  $\tilde{T}_{bx}$  and  $\tilde{T}_{by}$  are the  $\tilde{x}$  and  $\tilde{y}$  components of the bed shear stress vector  $\tilde{T}_b$ , respectively.  
 92 Though the bed friction coefficient  $C_f$  is a weak function of the flow depth relative to the roughness  
 93 height, it is assumed to be constant and common in both the vegetated and non-vegetated zones for  
 94 simplicity.

95 The vegetation drag stress vector  $\tilde{D}$  is described by the expression

$$96 \quad \tilde{D} = (\tilde{D}_x, \tilde{D}_y) = \begin{cases} 0 & \text{if } 0 \leq \tilde{y} \leq \tilde{B}, \\ \frac{\tilde{\rho} C_d \tilde{a} \tilde{H}}{2} (\tilde{U}^2 + \tilde{V}^2)^{1/2} (\tilde{U}, \tilde{V}) & \text{if } -\tilde{B}_v \leq \tilde{y} \leq 0, \end{cases} \quad (3)$$

97 where  $\tilde{D}_x$  and  $\tilde{D}_y$  are the components of the vector  $\tilde{D}$  in the  $\tilde{x}$  and  $\tilde{y}$  directions, respectively,  $C_d$  is  
 98 the drag coefficient of vegetation, typically estimated to range from 1 to 2, and  $\tilde{a} = \tilde{d}/(2\tilde{l}_x\tilde{l}_y)$  is the

99 parameter which describes the density of vegetation, where  $\tilde{d}$  is the diameter of the cylinders and  
 100  $\tilde{l}_x$  and  $\tilde{l}_y$  are the distances between the center of two adjacent cylinders in the  $\tilde{x}$  and  $\tilde{y}$  directions,  
 101 respectively, as shown in Figure 1.

102 It is assumed that, in the base state before instability occurs, the flow is already affected by  
 103 turbulence, which would be smaller in the length scale than the flow depth (sub-depth scale turbu-  
 104 lence). Where there is no influence of vegetation, the kinematic eddy viscosity  $\tilde{\nu}_T$  should corre-  
 105 spond to the sub-depth scale turbulence generated by the bottom friction. The logarithmic velocity  
 106 distribution is employed to represent the sub-depth scale turbulent velocity distribution affected  
 107 by the bottom friction. The kinematic eddy viscosity then takes a parabolic form, which is depth-  
 108 averaged from the bottom to the water surface, yielding (Fischer et al. 1979; Lima and Izumi  
 109 2014a)

$$110 \quad \tilde{\nu}_T = \frac{1}{6} \kappa \tilde{U}_f \tilde{H}_\infty, \quad (4)$$

111 where  $\tilde{U}_f (= \sqrt{\tilde{T}_{bx\infty}/\tilde{\rho}})$  and  $\tilde{H}_\infty$  are the friction velocity and the flow depth in the region suffi-  
 112 ciently far from the vegetated zone (denoted by the subscript  $\infty$ ), respectively, and  $\kappa$  is the Kármán  
 113 constant ( $= 0.4$ ). The sub-depth scale turbulence is assumed as isotropic. Therefore, the above for-  
 114 mulation is expected to describe the Reynolds stresses also in the streamwise and lateral directions  
 115 at a sufficient distance from the vegetated zone.

116 In the shear layer formed around the boundary between the two zones, and inside the vegetated  
 117 zone, the velocity and the shear velocity are reduced because of the Reynolds stress and the drag  
 118 force due to vegetation. In addition, the length scale of sub-depth scale vortices may be affected  
 119 by a typical length scale of vegetation, such as the spacing of the vegetation. According to the  
 120 experimental results of Ikeda et al. (1991), however, the depth-averaged kinematic eddy viscosity  
 121 even in the shear layer and the vegetated zone can be represented by equation (4). This may be  
 122 attributed to the fact that the sum of the resistant forces (the bed shear stress, the Reynolds stress  
 123 and the vegetation drag force) remains constant regardless of the reduction in the bed shear stress in  
 124 the shear layer and the vegetated zone. The kinematic eddy viscosity may be correlated to the total  
 125 resistant force. Furthermore, since the flow depth and the spacing of vegetation in the experiments

126 carried out by Ikeda et al. (1991) are both in the same range, it may well be that the kinematic eddy  
 127 viscosity in the vegetated zone is not strongly affected by vegetation. These assumptions and (4)  
 128 are employed in this study as well.

129 Fischer et al. (1979) determined the transverse mixing coefficient  $\varepsilon_t \cong 0.15\tilde{U}_f\tilde{H}$  from an  
 130 approximate average of experimental results in straight rectangular channels from various studies,  
 131 stating that the above result is likely to be correct for practical purposes in straight rectangular  
 132 channels with an error bound of  $\pm 50\%$ . Based on Fischer et al. (1979), Chen and Jirka (1997),  
 133 followed by Ghidaoui and Kolylshkin (1999) and Prooijen and Uijtewaal (2002), have assumed  
 134 values of kinematic eddy viscosity in the range  $\tilde{\nu}_t = 0.15-0.20\tilde{U}_f\tilde{H}$  for expressing the Reynolds  
 135 stress corresponding to the small-scale motions. This range of values of kinematic eddy viscosity  
 136 is, however, affected by the transverse mixing of the shear layer. On the other side, the eddy  
 137 viscosity in equation (4) is estimated for the flow without the transverse mixing generated by the  
 138 shear layer. Thus, it assumes a value smaller than  $\tilde{\nu}_t = 0.15-0.20\tilde{U}_f\tilde{H}$ . By employing (4) in the  
 139 formulation, a base flow consisting of the flow completely undisturbed by the lateral motions due  
 140 to the development of the shear layer can be derived.

141 The channel is assumed to be sufficiently wide to accommodate a shear layer which does not  
 142 reach the side walls. Under this assumption, it follows that the transverse velocity  $\tilde{V}$  vanishes and  
 143 the streamwise velocity  $\tilde{U}$  asymptotically approaches to constant slip velocities at the side walls of  
 144 the channel. The following boundary conditions therefore hold:

$$145 \quad \tilde{V} = 0 \quad \text{at} \quad \tilde{y} = -\tilde{B}_v, \tilde{B}, \quad (5a)$$

$$146 \quad \frac{\partial \tilde{U}}{\partial \tilde{y}} = 0 \quad \text{at} \quad \tilde{y} = -\tilde{B}_v, \tilde{B}. \quad (5b)$$

148 Right at the boundary between the non-vegetated and vegetated zones, the velocities, the flow  
 149 depth and the shear stresses are continuous, such that the following matching conditions hold:

$$150 \quad \lim_{\tilde{y} \rightarrow +0} \left( \tilde{U}, \frac{\partial \tilde{U}}{\partial \tilde{y}}, \tilde{H} \right) = \lim_{\tilde{y} \rightarrow -0} \left( \tilde{U}, \frac{\partial \tilde{U}}{\partial \tilde{y}}, \tilde{H} \right). \quad (6)$$

151 The above conditions are valid provided the vegetation is not sufficiently dense for a stress jump  
 152 to take place at  $\tilde{y} = 0$ .

153 It is assumed that at a sufficient distance from the boundary between the non-vegetated and  
 154 vegetated zones, the  $\tilde{x}$ -direction derivatives vanish, along with the  $\tilde{y}$  direction velocity component  
 155  $\tilde{V}$ . This yields a constant flow depth  $\tilde{H}_0 = \tilde{H}_\infty$ . At  $\tilde{y} = \tilde{B}$  and  $y = -\tilde{B}_v$ , the far field velocities,  
 156 denoted as  $\tilde{U}_\infty$  and  $\tilde{U}_{-\infty}$ , respectively, take the form

$$\tilde{U}_\infty = \left( \frac{\tilde{g}\tilde{H}_\infty S}{C_f} \right)^{1/2}, \quad \tilde{U}_{-\infty} = \left( \frac{2\tilde{g}\tilde{H}_\infty S}{2C_f + C_d\tilde{a}\tilde{H}_\infty} \right)^{1/2}, \quad (7a, b)$$

157 where the subscript  $-\infty$  denotes the far field in the vegetated zone. In experiments, the bed friction  
 158 coefficient  $C_f$  and the vegetation drag coefficient  $C_d$  can be determined from the above equations  
 159 once  $\tilde{U}_\infty$ ,  $\tilde{U}_{-\infty}$  and  $\tilde{H}_\infty$  are measured.

160 The velocity  $\tilde{U}_\infty$ , the flow depth  $\tilde{H}_0$  and the non-vegetated zone with  $\tilde{B}$  are taken as the char-  
 161 acteristic velocity, vertical length scale and horizontal length scale, respectively, for normalization,  
 162 which is introduced in the form

$$\tilde{\mathbf{U}} = \tilde{U}_\infty \mathbf{U}, \quad \tilde{H} = \tilde{H}_0 H, \quad (\tilde{x}, \tilde{y}, \tilde{B}_v) = \tilde{B}(x, y, B_v), \quad \tilde{t} = \frac{\tilde{B}}{\tilde{U}_\infty} t. \quad (8a, b, c, d)$$

163 With the use of the above normalization expressions, the governing equations (1) are rewritten in  
 164 the form

$$\frac{\partial \mathbf{U}}{\partial t} + (\mathbf{U} \cdot \nabla) \mathbf{U} = -F^2 \nabla H + \beta \left( \mathbf{g} - \frac{\mathbf{T}_b + \mathbf{D}}{H} \right) + \epsilon \nabla^2 \mathbf{U}, \quad (9a)$$

$$\frac{\partial H}{\partial t} + \nabla \cdot (H\mathbf{U}) = 0, \quad (9b)$$

167 where  $F$  is the Froude number,  $\beta$  is the bed-friction parameter and  $\epsilon$  is the sub-depth kinematic  
 168 eddy viscosity parameter, expressed in the forms

$$F = \frac{\tilde{U}_\infty}{\sqrt{\tilde{g}\tilde{H}_0}} = \left( \frac{S}{C_f} \right)^{1/2}, \quad \beta = \frac{C_f \tilde{B}}{\tilde{H}_0}, \quad \epsilon = \frac{\tilde{\nu}_T}{\tilde{U}_\infty \tilde{B}} = \frac{C_f^{1/2} \tilde{H}_0}{15 \tilde{B}}. \quad (10a, b, c)$$

169 The non-dimensional gravity vector  $\mathbf{g}$ , bed shear stress vector  $\mathbf{T}_b$  and vegetation drag vector  $\mathbf{D}$   
 170 take the forms:

$$171 \quad \mathbf{g} = (1, 0), \quad (11a)$$

$$172 \quad \mathbf{T}_b = (T_{bx}, T_{by}) = (U^2 + V^2)^{1/2} (U, V), \quad (11b)$$

$$173 \quad \mathbf{D} = (D_x, D_y) = \begin{cases} 0 & \text{if } 0 \leq y \leq 1, \\ \alpha (U^2 + V^2)^{1/2} H(U, V) & \text{if } -B_v \leq y \leq 0, \end{cases} \quad (11c)$$

174 where the non-dimensional parameter  $\alpha$  is related to the vegetation drag and density, and is defined  
 175 by

$$176 \quad \alpha = \frac{C_d \tilde{a} \tilde{H}_0}{2C_f}. \quad (12)$$

### 177 **Asymptotic expansions and the base flow solution**

178 The flow velocity components  $U$  and  $V$  and the flow depth  $H$  are decomposed into a base state  
 179 of order  $O(1)$  and a perturbed component of order  $O(A)$  in the form:

$$180 \quad \begin{pmatrix} U(x, y, t) \\ V(x, y, t) \\ H(x, y, t) \end{pmatrix} = \begin{pmatrix} U_0(y) \\ 0 \\ 1 \end{pmatrix} + A \begin{pmatrix} U_1(y) \\ V_1(y) \\ H_1(y) \end{pmatrix} e^{i(kx - \omega t)}, \quad (13)$$

181 where  $A$ ,  $k$  and  $\omega$  are the amplitude, wavenumber and angular frequency of the disturbance intro-  
 182 duced to the base flow, respectively.

183 The base state flow field is set as the flow undisturbed by the horizontal vortices. Because it  
 184 has only a streamwise component, it follows that the time and space derivatives and the transverse  
 185 velocity vanish and the flow depth is equal to unity. Substituting the terms of order  $O(1)$  from (13)  
 186 into (9) yields

$$187 \quad \beta (1 - U_0^2) + \epsilon \frac{d^2 U_0}{dy^2} = 0 \quad \text{if } 0 \leq y \leq 1, \quad (14a)$$

$$188 \quad \beta [1 - U_0^2 (1 + \alpha)] + \epsilon \frac{d^2 U_0}{dy^2} = 0 \quad \text{if } -B_v \leq y \leq 0. \quad (14b)$$

189 The analytical solution of (14) under the normalized forms of the boundary and matching  
 190 conditions (5)–(6) yields the following explicit expressions of  $U_0$ :

$$U_0(y) = \begin{cases} 3 \tanh^2 \left[ \left( \frac{\beta}{2\epsilon} \right)^{1/2} y + \tanh^{-1} \left( \frac{\psi + 2}{3} \right)^{1/2} \right] - 2 & \text{if } 0 \leq y \leq 1, \\ 3\phi \coth^2 \left[ - \left( \frac{\beta}{2\epsilon\phi} \right)^{1/2} y + \coth^{-1} \left( \frac{\psi + 2\phi}{3\phi} \right)^{1/2} \right] - 2\phi & \text{if } -B_v \leq y \leq 0, \end{cases} \quad (15)$$

191  
 192 where  $\phi$  is the normalized base flow velocity in the vegetated zone sufficiently far from the interface  
 193 with the non-vegetated zone and  $\psi$  is the normalized base flow velocity at the interface between  
 194 the non-vegetated and vegetated zones ( $y = 0$ ). The parameters  $\phi$  and  $\psi$  are explicit functions of  
 195 the vegetation drag and density parameter  $\alpha$  in the forms:

$$\phi = \frac{1}{(1 + \alpha)^{1/2}}, \quad \psi = \left[ \frac{2}{1 + \alpha + (1 + \alpha)^{1/2}} \right]^{1/3}. \quad (16a, b)$$

196 The domain of  $\phi$  is  $0 < \phi \leq 1$ ;  $\phi$  approaches 0 when the vegetation obstructs the flow completely  
 197 in the vegetated zone ( $\alpha \rightarrow \infty$ ), and takes a value of unity when there is no vegetation ( $\alpha = 0$ ).

198 The base flow velocity  $U_0$  is expressed by squared hyperbolic-tangent and squared hyperbolic-  
 199 cotangent functions which are invariant in time and in the streamwise direction and include four  
 200 non-dimensional parameters,  $\beta$ ,  $\epsilon$ ,  $\psi$  and  $\phi$ , where the latter two can be expressed as functions of  
 201 only  $\alpha$ . Fig. 2 depicts sample base state velocity profiles for various values of the eddy viscosity  
 202 parameter  $\epsilon$ . The velocities at the far right and left correspond to  $\tilde{U}_\infty$  and  $\tilde{U}_{-\infty}$  respectively, and  
 203 the value of  $U_0$  at the far left is  $\phi$ .

204 The base flow assumption herein consists of the flow undisturbed by the large scale vortices,  
 205 which is remarkably distinct from previous approaches (e.g. Michalke (1964, 1965), Chu et al.  
 206 (1991), Prooijen and Uijttewaai (2002), White and Nepf (2007)) where the base flow is set as the  
 207 average flow and for which the velocity distribution is fit to a hyperbolic tangent profile. The  
 208 lateral distributions of the base flow velocity  $U_0$  and the normalized measured streamwise velocity  
 209  $U$  at the developed state of the perturbations are depicted in Fig. 3 for run 1 of the experiments

210 of Ikeda et al. (1991), where vortices were generated in an open-channel featuring a lateral array  
 211 of regularly spaced cylinders, which is the same set-up assumed in the present formulation. As  
 212 expected, the shear layer is narrower in the base flow rather than in the developed average flow.  
 213 The shear layer widens as the perturbations grow nonlinearly. This study is, however, limited to  
 214 the linear reach of the perturbation development.

215 The velocity reduction in the boundary layer at the vicinity of the side walls, clearly visualized  
 216 in Fig. 3 at the far field in the non-vegetated zone, is not considered in the present analytical  
 217 model because it would virtually not affect the shear layer, since the channel is considered to be  
 218 sufficiently wide.

## 219 LINEAR STABILITY ANALYSIS

220 The substitution of (13) into the normalized governing equations (9) yields the following per-  
 221 turbed equations in the non-vegetated zone:

$$222 \left[ i(kU_0 - \omega) + k^2\epsilon + 2\beta U_0 - \epsilon \frac{d^2}{dy^2} \right] U_1 + \frac{dU_0}{dy} V_1 + (ikF^{-2} - \beta U_0^2) H_1 = 0, \quad (17a)$$

$$223 \left[ i(kU_0 - \omega) + k^2\epsilon + \beta U_0 - \epsilon \frac{d^2}{dy^2} \right] V_1 + F^{-2} \frac{dH_1}{dy} = 0, \quad (17b)$$

$$224 ikU_1 + \frac{dV_1}{dy} - i(\omega - kU_0)H_1 = 0, \quad (17c)$$

225 and the following perturbed equations in the vegetated zone,

$$226 \left[ i(kU_0 - \omega) + k^2\epsilon + 2\beta U_0(1 + \alpha) - \epsilon \frac{d^2}{dy^2} \right] U_1 + \frac{dU_0}{dy} V_1 + (ikF^{-2} - \beta U_0^2) H_1 = 0, \quad (18a)$$

$$228 \left[ i(kU_0 - \omega) + k^2\epsilon + \beta U_0(1 + \alpha) - \epsilon \frac{d^2}{dy^2} \right] V_1 + F^{-2} \frac{dH_1}{dy} = 0, \quad (18b)$$

$$230 ikU_1 + \frac{dV_1}{dy} - i(\omega - kU_0)H_1 = 0. \quad (18c)$$

231

232 Because the amplitude of the perturbations  $A$  is assumed to be infinitesimally small in the scheme  
 233 of linear stability analysis, terms containing  $A^2$  were dropped from (17–18).

234 A numerical scheme is necessary to solve (17–18) under the corresponding expanded forms of  
 235 the boundary and matching conditions (5–6), as the resulting system of equations obviously does  
 236 not allow analytical solutions. A spectral collocation method with the Chebyshev polynomials is  
 237 employed. In the non-vegetated zone ( $0 \leq y \leq 1$ ), the variables  $U_1$ ,  $V_1$  and  $H_1$  are expanded in the  
 238 form

$$239 \quad U_1 = \sum_{j=0}^N a_j T_j(\xi), \quad V_1 = \sum_{j=0}^N a_{(N+1)+j} T_j(\xi), \quad H_1 = \sum_{j=0}^N a_{2(N+1)+j} T_j(\xi), \quad (19)$$

240 and in the vegetated zone ( $-B_v \leq y \leq 0$ ), these variables are expanded in the form

$$241 \quad U_1 = \sum_{j=0}^N a_{3(N+1)+j} T_j(\gamma), \quad V_1 = \sum_{j=0}^N a_{4(N+1)+j} T_j(\gamma), \quad H_1 = \sum_{j=0}^N a_{5(N+1)+j} T_j(\gamma), \quad (20)$$

242 where  $a_j$  ( $j = 0, 1, 2, \dots, 6N + 5$ ) are the coefficients of the Chebyshev polynomials, and  $T_j(\xi)$   
 243 and  $T_j(\gamma)$  are the Chebyshev polynomials in  $\xi$  and  $\gamma$  of degree  $j$  respectively. The independent  
 244 variables  $\xi$  and  $\gamma$  both range from -1 to 1, and are related to  $y$  by the equations  $\xi = 2y - 1$   
 245 ( $0 \leq y \leq 1$ ) and  $\gamma = 2y/B_v + 1$  ( $-B_v \leq y \leq 0$ ), respectively. The expansions (19) and (20) are  
 246 substituted into the governing equations (17) and (18) respectively, and the resulting six equations  
 247 are evaluated at the Gauss-Lobatto points defined by

$$248 \quad \xi_m = \cos \frac{m\pi}{N}, \quad \gamma_m = \cos \frac{m\pi}{N}, \quad (21)$$

249 where  $m = 0, 1, \dots, N$ . Therefore, the number of points where the governing equations are eval-  
 250 uated is  $N + 1$ . A system of  $6(N + 1)$  algebraic equations with  $6(N + 1)$  unknown coefficients  
 251  $a_0, a_1, a_2, \dots, a_{6N+5}$  is obtained. Eight equations of the system are then replaced by the four bound-  
 252 ary conditions (5) and four of the matching conditions (6). The resulting linear algebraic system  
 253 takes the form

$$254 \quad \mathcal{M}\mathbf{A} = 0, \quad (22)$$

255 where  $\mathcal{M}$  is a  $6(N + 1) \times 6(N + 1)$  matrix in which the elements are derived from the coefficients  
 256 of  $U_1$ ,  $V_1$  and  $H_1$  in the governing equations (17–18) and the boundary and matching conditions  
 257 (5–6), and  $\mathbf{A} = [a_0, a_1, \dots, a_{6N+5}]^T$ . The condition for (22) to have a non-trivial solution is that  
 258  $\mathcal{M}$  should be singular. Thus,

$$259 \quad |\mathcal{M}| = 0. \quad (23)$$

260 Under the temporal framework of stability analysis, it is assumed that, in the present set up, the  
 261 domain of the streamwise direction  $\tilde{x}$  is sufficiently long to contain one or more complete periods  
 262 of a spatially periodic disturbance. The amplitude of this disturbance grows as time progresses.  
 263 Under the spatial framework, on the other hand, the disturbances are assumed to be generated at a  
 264 fixed position which, in the present set up, would correspond to the upstream boundary condition  
 265 of the partially vegetated channel. And the amplitude of the disturbances grows in the downstream  
 266 direction (Schmid and Henningson (2001)).

267 Although the spatial analysis is more complex because the eigenvalue appears nonlinearly,  
 268 there are physical situations, such as harmonic point sources, which require the modeling of the  
 269 disturbance amplitude as a spatially growing quantity (Schmid and Henningson (2001)). For mix-  
 270 ing layers, both temporal and spatial approaches have led to reasonable results, though only the  
 271 latter has been regarded for accounting for cross-stream distributions, in the case of an inviscid  
 272 hyperbolic-tangent base flow (Michalke (1964), Michalke (1965), Freymuth (1966), Ho and Huerre  
 273 (1984)), which is distinct from the base flow in the present work.

274 In the scheme of temporal linear stability analysis, the wavenumber is real, and is denoted as  
 275  $k^t = k_r^t$ , while the angular frequency is complex such that  $\omega^t = \omega_r^t + i\omega_i^t$ , where  $\omega_r^t$  is the real  
 276 angular frequency and  $\omega_i^t$  is the growth rate of the disturbance in time. As time progresses, the  
 277 perturbation grows if  $\omega_i^t > 0$  and decays if  $\omega_i^t < 0$ . In the temporal analysis, it is convenient to  
 278 decompose the matrix  $\mathcal{M}$  in the form

$$279 \quad \mathcal{M} = \mathcal{L}^t + \omega^t \mathcal{R}^t, \quad (24)$$

280 where the entries of  $\mathcal{L}^t$  are composed by the terms of the entries of  $\mathcal{M}$  which do not contain  $\omega^t$ ,  
 281 and the entries of  $\mathcal{R}^t$  are composed by the coefficients of  $\omega^t$  in the entries of  $\mathcal{M}$ . Substituting the  
 282 above decomposition into (22) yields the following generalized eigenproblem:

$$283 \quad \mathcal{L}^t \mathbf{A} = -\omega^t \mathcal{R}^t \mathbf{A}. \quad (25)$$

284 The solution of the above equation takes the functional form

$$285 \quad \omega^t = \omega^t(k^t, \beta, \epsilon, \alpha, B_v, F). \quad (26)$$

286 In the scheme of spatial linear stability analysis, on the other hand, the angular frequency is  
 287 real and is denoted as  $\omega^s = \omega_r^s$  while the wavenumber is complex as  $k^s = k_r^s + ik_i^s$ , where  $k_r^s$  is the  
 288 real wavenumber and  $k_i^s$  is the growth rate of the disturbance in space. In the case of a downstream  
 289 propagating disturbance, which is the case considered herein,  $k_i^s$  assumes negative values. In the  
 290 scope of spatial analysis, it is convenient to decompose the matrix  $\mathcal{M}$  in the form:

$$291 \quad \mathcal{M} = \mathcal{L}^s + k^s \mathcal{R}_1^s + k^{s2} \mathcal{R}_2^s, \quad (27)$$

292 where the entries of  $\mathcal{L}^s$  are composed by the terms of the entries of  $\mathcal{M}$  which do not contain  $k^s$  (or  
 293  $k^{s2}$ ), and  $\mathcal{R}_1$  and  $\mathcal{R}_2$  are composed by the coefficients of  $k^s$  and  $k^{s2}$ , respectively, in the entries of  
 294  $\mathcal{M}$ . Substituting the above decomposition into (22) yields the following nonlinear eigenproblem:

$$295 \quad \mathcal{L}^s \mathbf{A} = - (k^s \mathcal{R}_1^s + k^{s2} \mathcal{R}_2^s) \mathbf{A}. \quad (28)$$

296 The above expression is linearized in the form

$$297 \quad \begin{pmatrix} \mathcal{L}^s & 0 \\ 0 & I \end{pmatrix} \begin{pmatrix} \mathbf{A} \\ k^s \mathbf{A} \end{pmatrix} = k^s \begin{pmatrix} -\mathcal{R}_1^s & -\mathcal{R}_2^s \\ I & 0 \end{pmatrix} \begin{pmatrix} \mathbf{A} \\ k^s \mathbf{A} \end{pmatrix}. \quad (29)$$

298 where  $I$  is the identity matrix. The solution of the above equation takes the functional form

$$299 \quad k^s = k^s(\omega^s, \beta, \epsilon, \alpha, B_v, F). \quad (30)$$

## 300 RESULTS AND DISCUSSION

301 Unless otherwise specified, the parameters  $\beta$ ,  $\epsilon$ ,  $\alpha$ ,  $B_v$  and  $F$  are kept fixed at  $\beta = 0.05$ ,  
 302  $\epsilon = 6 \times 10^{-4}$ ,  $\alpha = 10$ ,  $B_v = 0.55$  and  $F = 0.5$ . This set of values is based on typical values of  
 303 the experiments of Ikeda et al. (1991). Also,  $N = 30$  was adopted in the Chebyshev polynomials,  
 304 with results independent of the numerical resolution.

### 305 Spectral analysis

306 In the temporal problem, the eigenvalue  $\omega^t$  with the largest imaginary part  $\omega_i^t$  is selected to  
 307 compute the temporal growth rate of perturbation. Fig. 4(a) depicts the temporal spectrum for the  
 308 case  $k_r^t = 5.0$ , where there is a single eigenvalue which corresponds to temporal growth ( $\omega_i^t > 0$ ),  
 309 located in the range of positive  $\omega_r^t$ . Fig. 4(b) displays the spatial spectrum for the case  $\omega_r^s =$   
 310  $3.2$ . Differently from the temporal spectrum, the spatial spectrum contains eigenvalues in all four  
 311 quadrants.

312 Fig. 5 depicts instability diagrams for the temporal case. In Fig. 5(a), the temporal growth rate  
 313 is positive for the range  $0.92 \leq k^t \leq 12.78$ , which corresponds to the range  $0.56 \leq \omega_r^t \leq 7.53$ ,  
 314 as depicted in Fig. 5(b). Therefore, the neutral cases where the imaginary parts of  $\omega$  and  $k$  are  
 315 both equal to zero correspond to  $(k, \omega) = (0.92, 0.56)$  and  $(k, \omega) = (12.78, 7.53)$ . When selecting  
 316 eigenvalues for computing spatial growth,  $k_r^s$  and  $\omega_r^s$  must then be same ranges of  $k_r^t$  and  $\omega_r^t$  for  
 317 which temporal growth takes place. Additionally,  $k_i^s$  must be negative because the disturbance  
 318 propagates downstream.

### 319 Evaluation of the perturbation growth

320 Following Gaster (1962), the spatial growth rate  $k_i^s$  can be alternatively determined from the  
 321 temporal analysis as

$$322 \quad k_i^s = -\frac{\omega_i^t}{c_g^t}, \quad (31)$$

323 where  $c_g = \partial\omega_r/\partial k_r$  is the group velocity.

324 Fig. 6 depicts instability diagrams of the spatial growth rate  $-k_i^s$  determined from the temporal  
325 and the spatial analyses. The curves of the temporal and spatial analyses are roughly similar, with  
326 a small discrepancy observed in the range of large values of  $-k_i^s$ . This discrepancy is expected  
327 because (31) is obtained assuming that the terms of order  $O(\max(\omega_i^{t^2}))$  are negligible (Gaster  
328 1962). The maximum spatial growth rate in the temporal curve is  $-k_i^s = 0.878$  and takes place at  
329  $\omega_r^t = 3.76$ , while the maximum growth rate in the spatial curve is  $-k_i^s = 0.898$  and is located at  
330  $\omega_r^s = 3.67$ . For comparison, the maximum temporal growth in Fig. 5 ( $\omega_i^t = 0.519$ ) takes place at  
331  $\omega_r^t = 3.45$ .

332 Fig. 7 depicts the contours of the spatial growth rate  $-k_i^s$ , determined from the temporal and  
333 the spatial analyses, in the  $\epsilon-k_r$  plan. The contours of the neutral instability ( $k_i = 0$ ) are obvi-  
334 ously coincident. As the absolute value of the growth rates increase, the discrepancy between the  
335 contours obtained from the temporal and the spatial analyses becomes more significant.

336 The results of this study indicate that the frequencies corresponding to the maximum amplifi-  
337 cation in space are slightly larger (if not virtually equal) than those corresponding to the maximum  
338 amplification in time. Ikeda et al. (1991, 1994), Tsujimoto (1991) and White and Nepf (2007,  
339 2008) performed experiments (Table 1) where vortices were generated in an open-channel featur-  
340 ing a lateral array of regularly spaced pile dikes, which is the same set up assumed in the present  
341 formulation. Lima and Izumi (2014a) predicted the period of vortex shedding associated with  
342 the maximum amplification in time for the experimental cases of Ikeda et al. (1991, 1994) and  
343 Tsujimoto (1991). The predicted period was approximately 50% of the period observed in the  
344 experiments, owing to the fact that the linear stability analysis describes the onset of instability  
345 while the experimental measurements were obtained for the developed stage of perturbations. The  
346 predicted vortex shedding frequencies associated with the maximum growth in space would then  
347 be slightly smaller than those from the temporal case, if not virtually equal.

348 According to Ho and Huerre (1984), the Strouhal number of the most amplified wave in a free  
349 shear layer prior to the nonlinear development of instabilities,  $St = \tilde{\omega}_m \tilde{\theta} / \tilde{U}_a$ , takes the nearly con-

350 stant value of 0.032 for any hyperbolic tangent base flow profile, where  $\tilde{\omega}_m$  is the natural frequency  
 351 of the maximum instability,  $\tilde{U}_a$  is the average of the far field velocities,  $\tilde{U}_a = (\tilde{U}_\infty + \tilde{U}_{-\infty})/2$ , and  
 352  $\tilde{\theta}$  is the momentum thickness of the undisturbed flow. Ho and Huerre (1984) also noted that the  
 353 Strouhal number of the most amplified wave in a free shear layer drops significantly below the neu-  
 354 tral value of 0.032 as the flow develops and nonlinear interactions become important. Lima and  
 355 Izumi (2014b) determined the Strouhal number based on the most amplified wave determined from  
 356 the temporal linear stability analysis and the momentum thickness calculated from the base flow  
 357 velocity solution (15) for the experimental runs of Ikeda et al. (1991) and White and Nepf (2007,  
 358 2008). Results were within the range  $0.034 \leq St \leq 0.042$ . In the case of the spatial analysis, the  
 359 range determined herein is  $0.035 \leq St \leq 0.046$ . The slight overestimation from the present for-  
 360 mulation in either the temporal or spatial approach may be because the base flow velocity in (15)  
 361 is set completely free of the transverse motions of the shear layer, while the hyperbolic-tangent  
 362 velocity profile, for which  $St \approx 0.032$ , may have effects of such transverse motions.

### 363 **Evaluation of the phase velocity**

364 Fig. 8 depicts curves of the phase velocity  $c_p = \omega_r/k_r$  as a function of the frequency  $\omega_r$  for the  
 365 temporal and spatial cases and for multiples values of  $\beta$ ,  $\epsilon$ ,  $\alpha$ ,  $B_v$ ,  $F$  and  $\tilde{B}/\tilde{H}_0$ .

366 In Michalke (1964, 1965), the phase velocity in the temporal approach is constant and equal to  
 367 the group velocity, whereas the phase velocity in the spatial case varies strongly with the frequency  
 368  $\omega_r$ , especially for small values of  $\omega_r$ . Michalke (1965) stated that the behavior of the phase velocity  
 369 in the spatial predictions was observed in the experiments of Freymuth (1965).

370 In the present work, however, the phase velocity in the temporal problem is not constant, as  
 371 seen in Fig. 8. A clear discrepancy can be noted between the curves of  $c_p^t$  and  $c_p^s$ , mainly in  
 372 the range of frequencies smaller than that where the spatial and temporal curves intersect. The  
 373 curves in the temporal and spatial cases intersect near the points where  $\omega_i$  and  $-k_i$  are maximized.  
 374 Therefore, the preferential frequencies for maximum amplification in time and space converge to  
 375 approximately the same value. Moreover, the values of  $c_p$  in the temporal and spatial cases at the  
 376 minimum  $\omega_r$  for instability tend to converge. This differs remarkably from the results of Michalke

377 (1964, 1965). In the present work, the minimum frequency for an unstable flow corresponds to  
378 the same phase velocity  $c_p$ , regardless of the approach (spatial or temporal) taken. This is because  
379 the base flow is set as the flow completely free from the instabilities due to the shear layer. As the  
380 frequency grows, the curves of  $c_p$  in the spatial and temporal cases often follow distinct paths until  
381 they intersect at the vicinity of the frequencies for maximum amplification.

382 The frequency for maximum amplification increases significantly as the bed friction parameter  
383  $\beta$  increases and the kinematic eddy viscosity parameter  $\epsilon$  decreases, as depicted in Fig. 8(a) and (b),  
384 respectively. Additionally, the discrepancy between  $c_p$  in the temporal and spatial cases becomes  
385 more significant as the value of  $\omega_r$  at the intersection increases.

386 The vegetation drag parameter  $\alpha$  has a strong effect on  $c_p$ , as depicted in Fig. 8(c). For  $\alpha = 10^0$ ,  
387 the instability is characterized by long waves (small  $k_r$ ) moderately amplified, as seen in Fig. 9.  
388 For  $\alpha = 10^1$ , the range of  $k_r$  for unstable flow reaches higher values; therefore shorter waves are  
389 also commonplace as  $\alpha$  increases to  $10^1$ . The reduction of  $c_p$  for  $\alpha = 10^2$  and  $10^3$  may be attributed  
390 to the reduction in the domain of frequencies ( $\omega_r$ ) for unstable flow.

391 The discrepancy between  $c_p$  in the temporal and spatial cases is more significant for larger  
392 growth rates. In Fig. 8(b), the discrepancy of the temporal and spatial curves of  $c_p$  increases with  
393 decreasing values of  $\epsilon$ . As is verified in Fig. 7, the growth rates are larger for smaller values of  $\epsilon$ .  
394 Similarly, for  $\alpha = 10^1$  and  $10^2$ , a greater discrepancy is found in the curves of  $c_p$  (Fig. 8(c)) and  
395 the growth rates reach their maximum range (Fig. 9).

396 The effect of the non-dimensional vegetated zone width  $B_v$  on  $c_p$  is indicated in Fig. 8(d). The  
397 curves of  $c_p$  in the range of small  $\omega_r$  vary considerably between the temporal and spatial cases  
398 and between the values of  $B_v$ . For  $\omega_r$  larger than the frequency of maximum amplification, the  
399 temporal curves of  $B_v = 0.6$  and  $B_v = 1.0$  are virtually coincident. This was also the case for the  
400 spatial curves. When the values of  $B_v$  are sufficiently large, the maximum amplification is virtually  
401 independent of  $B_v$ . Because it is assumed that  $B_v$  is sufficiently large to achieve a constant far field  
402 velocity in the vegetated zone, the reliability of the results for  $B_v = 0.2$  is questionable, though it  
403 is presented to clarify the tendency of  $c_p$  at small  $B_v$ .

404 The effect of the Froude number  $F$  on  $c_p$  is depicted in Fig. 8(e). For  $F = 0.001$ ,  $F = 1.0$ ,  
 405 and  $F = 2.0$ , the flow is unstable due to the shear layer, and the results show features similar to  
 406 those from Fig. 8(a–d,f). For  $F = 3.0$ , on the other hand, the flow is unstable due to gravity, and  
 407 two modes of instability appear, which is verified by the two pairs of curves of  $c_p$ . For  $F = 3.0$ ,  
 408 the temporal and spatial curves are virtually coincident, as are the points where the perturbation  
 409 growth is maximized.

410 Finally, the effect of the aspect-ratio  $\tilde{B}/\tilde{H}_0$  on  $c_p$  is studied in Fig. 8(f). It is assumed that the  
 411 variation of the aspect-ratio is solely due to the variation of  $\tilde{B}$ , such that the parameters  $\alpha$  and  $F$   
 412 are kept fixed at  $\alpha = 10$  and  $F = 0.5$ , while  $\beta$  and  $\epsilon$  vary. The parameter  $B_v$  is kept fixed at  
 413  $B_v = 0.55$  assuming that the proportion of the widths on the non-vegetated and vegetated zones  
 414 does not vary. As the aspect-ratio increases,  $\beta$  increases, while  $\epsilon$  decreases, resulting in Fig. 8(f)  
 415 being somewhat similar to Fig. 8(a) and (b).

416 Fig. 10 depicts the phase velocity  $c_p$  versus the angular frequency  $\omega_r$  obtained from employing  
 417 a base flow velocity modified from Michalke (1964, 1965) expressed as

$$418 \quad U_0(y) = \phi + 0.5(1 - \phi)[1 + \tanh(\eta y)] \quad (32)$$

419 instead of the analytical solutions expressed in (15). In the above,  $\eta$  is introduced such that the  
 420 velocity profiles of (15) and (32) have the same shear layer width. The shear layer width is defined  
 421 based on the analytical solutions (15) as the distance along the transverse direction  $y$  from the  
 422 location where 99% of the velocity difference  $\psi - \phi$  is recovered to the location where 99% of  
 423 the velocity difference  $1 - \psi$  is recovered. The parameter  $\eta$  is therefore a function of  $\beta$ ,  $\epsilon$  and  
 424  $\alpha$ . In Fig. 10,  $\beta = 0.05$  and  $\epsilon = 6 \times 10^{-4}$ , for which  $\eta$  is determined to be 9.55 and 12.13 for  
 425  $\alpha = 10$  and 100, respectively. In Fig. 10(a), the parameters  $\beta$  and  $\epsilon$  are kept in the perturbation  
 426 equations (17–18). In Fig. 10(b),  $\epsilon$  is dropped from (17–18), while  $\beta$  is maintained. In Fig. 10(c),  
 427  $\beta$  is dropped while  $\epsilon$  is maintained and finally, in Fig. 10(d), both  $\beta$  and  $\epsilon$  are dropped. Fig. 10(d)  
 428 presents features notably similar to the results of Michalke (1964, 1965), such as 1)  $c_p$  constant and

429 equal to  $(\phi + 1)/2$  in the temporal case; 2) instability taking place from  $\omega_r \rightarrow 0$  and 3)  $c_p$  at the  
 430 minimum  $\omega_r$  for instability being remarkably distinct in the temporal and spatial cases. The first  
 431 and second features are also observed in Fig. 10(c). Therefore, the combined effect of parameters  
 432  $\beta$ ,  $\epsilon$  and  $\alpha$  causes the results of the present work to be distinct from those of Michalke (1964,  
 433 1965). Moreover, the effect of large Froude number  $F$  modifies the results considerably, as seen  
 434 in Fig. 8(e). In Fig. 10(a), although the parameters  $\beta$  and  $\epsilon$  are kept in the perturbation equations,  
 435 the curves are distinct from those of Fig. 8(c). In Figs. 10(a) and (b), the flow is stable at small  
 436 angular frequency  $\omega_r$  (as well as wavenumber  $k$ ) because the bed friction effect, expressed by the  
 437 parameter  $\beta$ , dumps small scale perturbations of the shear layer.

### 438 **Evaluation of the eigenfunction**

439 Michalke (1964, 1965) and Freymuth (1966) demonstrated that only the spatial analysis can  
 440 capture the distribution of the disturbance velocity component across the spanwise domain. In  
 441 particular, the temporal analysis carried out by Michalke (1964) resulted in symmetric and anti-  
 442 symmetric cross-distributions of the real and imaginary parts the eigenfunction, respectively. This  
 443 behavior was not observed in Michalke's (1965) spatial analysis, where the cross-distribution of the  
 444 real and imaginary parts of the eigenfunctions were asymmetric. Moreover, a sharp phase rever-  
 445 sal of the disturbance velocity component, observed in the experiments of Freymuth (1965), was  
 446 predicted by the spatial analysis by Michalke (1965), but not in the temporal analysis (Michalke  
 447 (1964)) except in the case of a neutral disturbance.

448 Fig. 11 depicts the real and imaginary parts as well as the absolute values of the eigenfunction  
 449  $U_1(y)$  determined in the present work across the spanwise domain. The eigenfunction is normal-  
 450 ized such that  $U_1(0) = 1$ . The temporal and spatial curves are obtained for the wavenumber and  
 451 frequency where the amplification is maximized, which correspond to  $(k^t, \omega_r^t) = (5.48, 3.45)$  in  
 452 the temporal case and  $(k_r^s, \omega^s) = (5.91, 3.70)$  in the spatial case. The cross-distributions of the  
 453 eigenfunction  $U_1(y)$  from both the temporal and spatial analyses are found to be asymmetric and  
 454 both contain sharp phase reversals at  $y \approx -0.1$  and  $y \approx 0.1$ . This differs from the results reported  
 455 by Michalke (1965).

## CONCLUSIONS

Temporal and spatial linear stability analyses of an open-channel flow covered with vegetation at one of its sides are performed. A viscous-flow approach was employed, with the Reynolds stress expressed by means of a kinematic eddy viscosity associated with sub-depth scale turbulences. As a result, a base flow consisting of the flow completely free from the effect of the transverse motions of the shear layer was derived. This is distinct from previous approaches where the base flow consisted of the average flow for which a hyperbolic-tangent velocity distribution was imposed. The average flow is affected by the increased mixing efficiency caused by the development of large scale turbulences in the shear layer. Thus, the results of the formulations used in this study may provide more reliable insight into the onset of instabilities in the shear layer, compared to these previous approaches.

In this work, less difference was found between the results from the temporal and spatial approaches than those from previous inviscid approaches. This may be attributed not only to the inclusion of the effect of the kinematic eddy viscosity in the present formulation, but also to the inclusion of the effects of bed shear, gravity and differential drag in the vegetated zone.

The phase velocity corresponding to the minimum angular frequency for instability was found to be approximately the same in both the temporal and spatial approaches. Moreover, the phase velocity was determined to be correlated to the frequency not only in the spatial case, but also in the temporal case. The frequency of the maximum amplification was found to be slightly smaller in the spatial case than in the temporal case (if not virtually equal). Finally, the cross-distribution of the streamwise velocity eigenfunction was found to be asymmetric for both the temporal and spatial cases.

The most noticeable difference between results from the temporal and spatial analyses may be attributed to the phase velocity in the range of small frequencies (excluding the vicinity of the minimum neutral frequency). This is more clearly observed in the case of small eddy viscosity parameter  $\epsilon$  and resembles the discrepancy between results from spatial and temporal linear stability analysis in inviscid shear layers.

## APPENDIX I. REFERENCES

- Carnie, R., Tonina, D., McKean, J. A., and Isaak, D. (2015). "Habitat connectivity as a metric for aquatic microhabitat quality: application to Chinook salmon spawning habitat." *Ecohydrology*, doi: 10.1002/eco.1696.
- Chen, D. and Jirka, G. H. (1997). "Absolute and convective instabilities of plane turbulent wakes in a shallow water layer." *Journal of Fluid Mechanics*, 338, 157–172.
- Chu, V. H., Wu, J.-H., and Khayat, R. E. (1991). "Stability of transverse shear flows in shallow open channels." *Journal of Hydraulic Engineering, ASCE*, 117(11), 1370–1388.
- Fischer, H. B., List, E. J., Koh, R. C. J., Imberger, J., and Brooks, N. H. (1979). *Mixing in Inland and Coastal Waters*. Academic, New York.
- Freytmuth, P. (1965). *Diss. Technische Universität Berlin (as cited in Michalke, 1965)*.
- Freytmuth, P. (1966). "On transition in a separated laminar boundary layer." *Journal of Fluid Mechanics*, 25, 683–704.
- Gaster, M. (1962). "A note on the relation between the temporally-increasing and spatially-increasing disturbances in hydrodynamic instability." *Journal of Fluid Mechanics*, 14, 222–224.
- Ghidaoui, M. S. and Kolyshkin, A. A. (1999). "Linear stability analysis of lateral motions in compound open channel." *Journal of Hydraulic Engineering, ASCE*, 125(8), 871–880.
- Ho, C.-M. and Huerre, P. (1984). "Perturbed free shear layers." *Annual Review of Fluid Mechanics*, 16, 365–424.
- Ikeda, S., Izumi, N., and Itoh, R. (1991). "Effects of pile dikes on flow retardation and sediment transport." *Journal of Hydraulic Engineering, ASCE*, 117(11), 1459–1478.
- Ikeda, S., Ohta, K., and Hasegawa, H. (1994). "Instability-induced horizontal vortices in shallow open-channel flows with an inflection point in skewed velocity profile." *Journal of Hydroscience and Hydraulic Engineering*, 12, 69–84.
- Kitamura, T., Jia, Y., Tsujimoto, T., and Wang, S. (1998). "Sediment transport capacity in channels with vegetation zone." *Water Resource Engineering '98*, S. R. Abt, J. Youngpezeshk, and C. C. Watson, eds., number 326, Baltimore, ASCE Publications.

510 Kolyshkin, A. A. and Ghidaoui, M. S. (2002). “Gravitational and shear instabilities in compound  
511 and composite channels.” *Journal of Hydraulic Engineering, ASCE*, 128(12), 1076–1086.

512 Lima, A. C. and Izumi, N. (2014a). “Linear stability analysis of open-channel shear flow generated  
513 by vegetation.” *Journal of Hydraulic Engineering, ASCE*, 140(3), 231–240.

514 Lima, A. C. and Izumi, N. (2014b). “On the nonlinear development of shear layers in partially  
515 vegetated channels.” *Physics of Fluids*, 26, 084109–1–084109–22.

516 Michalke, A. (1964). “On the inviscid instability of hyperbolic tangent velocity profile.” *Journal  
517 of Fluid Mechanics*, 19, 543–556.

518 Michalke, A. (1965). “On spatially growing disturbances in an inviscid shear layer.” *Journal of  
519 Fluid Mechanics*, 23, 521–544.

520 Monkewitz, P. A. and Huerre, P. (1982). “Influence of the velocity ratio on the spatial instability of  
521 mixing layers.” *Physics of Fluids*, 25, 1137–1143.

522 Nadaoka, K. and Yagi, H. (1998). “Shallow-water turbulence modeling and horizontal large-eddy  
523 computation of river flow.” *Journal of Hydraulic Engineering, ASCE*, 124(5), 493–500.

524 Prooijen, B. C. and Uijtewaal, W. S. J. (2002). “A linear approach for the evolution of coherent  
525 structures in shallow mixing layers.” *Physics of Fluids*, 14, 4105–4114.

526 Schmid, P. J. and Henningson, D. S. (2001). *Stability and transition in shear flows*. Springer.

527 Su, X. and Li, C. W. (2002). “Large eddy simulation of free surface turbulent flow in partially  
528 vegetated open channels.” *International Journal of Numerical Methods in Fluids*, 39, 919–937.

529 Tamai, N., Asaeda, T., and Ikeda, H. (1986). “Study on generation of periodical large surface  
530 eddies in a composite channel flow.” *Water Resources Research*, 22(7), 1129–1138.

531 Tsujimoto, T. (1991). “Open channel flow with bank vegetation.” *KHL Communication*, 2, 41–54.

532 Tsujimoto, T. and Kitamura, T. (1995). “Lateral bed-load transport and sand-ridge formation near  
533 vegetation zone in an open channel.” *Journal of Hydroscience and Hydraulic Engineering*, 35–  
534 45.

535 Uijtewaal, W. S. J. and Booij, R. (2000). “Effects of shallowness on the development of free-  
536 surface mixing layers.” *Physics of Fluids*, 12, 4392–4402.

- 537 White, B. L. and Nepf, H. M. (2007). “Shear instability and coherent structures in shallow flow  
538 adjacent to a porous layer.” *Journal of Fluid Mechanics*, 593, 1–32.
- 539 White, B. L. and Nepf, H. M. (2008). “A vortex-based model of velocity and shear  
540 stress in a partially vegetated shallow channel.” *Water Resources Research*, 44, W01412,  
541 doi:10.1029/2006WR005651.

**APPENDIX II. NOTATION**

*The following symbols are used in this paper:*

- $A$  = amplitude;  
 $a$  = vegetation density parameter;  
 $B$  = non-vegetated zone width;  
 $B_v$  = vegetated zone width;  
 $C_d$  = vegetation drag coefficient;  
 $C_f$  = bed friction coefficient;  
 $c_g$  = group velocity;  
 $c_p$  = phase velocity;  
 $D_x, D_y$  = streamwise and transverse vegetation drag components, respectively;  
 $d$  = diameter of cylinders;  
 $F$  = Froude number;  
 $g$  = gravity acceleration;  
 $H$  = flow depth;  
 $k$  = wavenumber;  
 $l_x, l_y$  = distances between the center of two adjacent cylinders in the  $x$  and  $y$  directions;  
 $S$  = streamwise bed slope of the channel;  
 $T_{bx}, T_{by}$  = streamwise and transverse bed shear stress components, respectively;  
 $T_j(\xi), T_j(\zeta)$  = Chebyshev polynomials in  $\xi$  and  $\zeta$  of degree  $j$ ;  
 $t$  = time;  
 $U, V$  = streamwise and transverse velocities, respectively;  
 $U_0$  = base state flow velocity;  
 $U_1, V_1, H_1$  = eigenfunctions;  
 $U_f$  = friction velocity;  
 $x, y$  = streamwise and transverse coordinates, respectively;  
 $\alpha$  = vegetation drag and density parameter;

- $\beta$  = bed friction parameter;
- $\epsilon$  = kinematic eddy viscosity parameter;
- $\kappa$  = Kármán constant;
- $\nu_T$  = kinematic eddy viscosity;
- $\rho$  = water density;
- $\phi$  = ratio between the undisturbed velocities in the vegetated zone and the non-vegetated zone;
- $\psi$  = base state flow velocity at the interface between the non-vegetated and vegetated zones; and
- $\omega$  = angular frequency.

544

*Subscripts:*

- $\infty, -\infty$  = far field in the non-vegetated and vegetated zones, respectively.

545 **List of Tables**

546 1 Hydraulic parameters for the experiments of Ikeda et al. (1991, 1994) (runs 1–5),

547 Tsujimoto (1991) (runs IW1–IW3) and White and Nepf (2007, 2008) (runs I–XI). . 27

TABLE 1: Hydraulic parameters for the experiments of Ikeda et al. (1991, 1994) (runs 1–5), Tsujimoto (1991) (runs IW1–IW3) and White and Nepf (2007, 2008) (runs I–XI).

Run	Discharge (l/s)	$\tilde{U}_\infty$ (cm/s)	$\tilde{U}_f$ (cm/s)	$\tilde{H}$ (cm)	$S$	$C_d \tilde{a}$ (cm <sup>-1</sup> )	$\beta$	$\epsilon$ ( $\times 10^{-4}$ )	$\alpha$	$B_v$	$F$
1	15.3	39.5	3.08	6.0	0.0010	0.020	0.061	5.19	9.87	0.57	0.51
2	22.6	58.8	4.58	6.0	0.0033	0.020	0.061	5.19	9.87	0.57	0.77
3	18.6	51.8	4.18	5.0	0.0033	0.018	0.079	4.48	6.89	0.57	0.74
4	7.0	33.7	3.04	3.0	0.0033	0.020	0.164	3.00	3.69	0.57	0.62
5	24.0	43.7	3.19	8.5	0.00067	0.020	0.038	6.88	16.0	0.57	0.48
IW1	-	41.6	2.31	3.7	0.0015	-	0.024	4.84	67.9	0.43	0.69
IW2	-	47.5	3.05	3.8	0.0025	-	0.030	5.84	50.8	0.43	0.78
IW3	-	57.0	3.34	3.9	0.0029	-	0.025	5.40	63.5	0.43	0.93
I	-	17.7	1.81	6.8	-	0.092	0.058	3.99	63.0	0.50	0.22
II	-	21.7	2.27	10.4	-	0.092	0.023	4.73	154	0.50	0.21
III	-	24.0	2.67	13.8	-	0.092	0.023	7.31	160	0.50	0.21
IV	-	17.4	2.06	6.6	-	0.285	0.064	4.02	192	0.50	0.22
V	-	3.8	0.35	5.3	-	0.242	0.061	2.82	232	0.50	0.05
VI	-	12.3	1.48	6.0	-	0.255	0.043	2.86	214	0.50	0.16
VII	-	16.8	1.93	6.6	-	2.43	0.055	3.73	1530	0.50	0.21
VIII	-	5.9	0.44	5.5	-	2.74	0.126	4.29	1520	0.50	0.08
IX	-	9.1	0.84	6.8	-	2.04	0.089	4.95	1310	0.50	0.11
X	-	29.6	3.44	7.8	-	1.77	0.066	5.22	1100	0.50	0.34
XI	-	22.0	2.51	13.9	-	2.43	0.032	8.70	2880	0.50	0.19

548  
549  
550  
551  
552  
553  
554  
555  
556  
557  
558  
559  
560  
561  
562  
563  
564  
565  
566  
567  
568  
569  
570  
571  
572  
573

## List of Figures

- 1 Conceptual diagram of the channel with vegetation. (a) The cross-sectional view, and (b) the plan view. . . . . 30
- 2 Lateral distribution of the base flow velocity  $U_0$  for the case  $\beta = 0.05$ ,  $\alpha = 10$  and variable sub-depth eddy viscosity parameter  $\epsilon$ . . . . . 31
- 3 Base state velocity  $U_0$  (continuous line) and measured streamwise velocity  $U$  at the developed state of perturbations along the lateral direction  $y$ , for run 1 of Ikeda et al. (1994), where  $\beta = 0.061$ ,  $\epsilon = 5.2 \times 10^{-4}$  and  $\alpha = 9.9$ . . . . . 32
- 4 (a) Temporal spectrum for  $k^t = 5.0$  and (b) spatial spectrum for  $\omega^s = 3.2$ . The arrows indicate the eigenvalues to be selected for computing the perturbation growth. 33
- 5 Instability diagrams for the temporal case: (a)  $\omega_i^t$  versus  $k^t$ ; (b)  $\omega_i^t$  versus  $\omega_r^t$ . . . . . 34
- 6 Spatial growth rates  $-k_i^s$  obtained from the temporal analysis (dashed line) and the spatial analysis (continuous line). . . . . 35
- 7 Contours of the spatial growth rate  $-k_i^s$  determined from (a) the temporal analysis (dashed lines) and (b) the spatial analysis (continuous lines) in the  $\epsilon$ - $k_r$  plane. . . . . 36
- 8 Phase velocity  $c_p$  versus angular frequency  $\omega_r$  for the temporal analysis (dashed lines) and the spatial analysis (continuous lines). The phase velocity and angular frequency at the maximum amplification are indicated by  $\square$  for the temporal analysis and by  $\blacksquare$  for the spatial analysis. . . . . 37
- 9 Contours of  $\omega_i$  (dashed lines) and  $-k_i$  (continuous lines) in the (a)  $\alpha$ - $k_r$  plane and  $\alpha$ - $\omega_r$  plane. . . . . 38
- 10 Phase velocity  $c_p$  versus angular frequency  $\omega_r$  for the temporal analysis (dashed lines) and the spatial analysis (continuous lines) calculated using the base flow velocity of equation (32). (a) Perturbation equations (17–18) not modified; (b)  $\epsilon$  dropped from (17–18); (c)  $\beta$  dropped from (17–18); (d)  $\beta$  and  $\epsilon$  dropped from (17–18). . . . . 39

574 11 Lateral distribution of the (a) real part, (b) imaginary part and (c) absolute value  
575 of eigenfunction  $U_1(y)$  at the maximum amplification in time (dashed curves) and  
576 space (continuous curves). . . . . 40

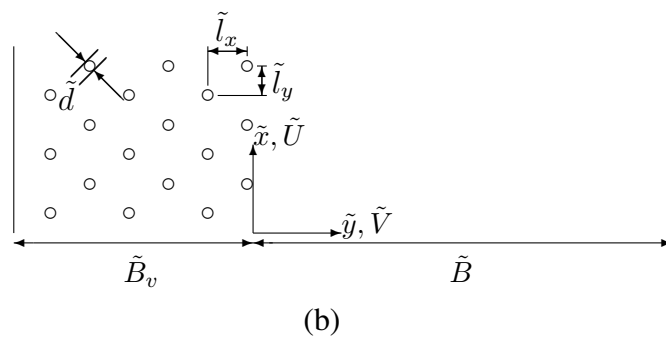
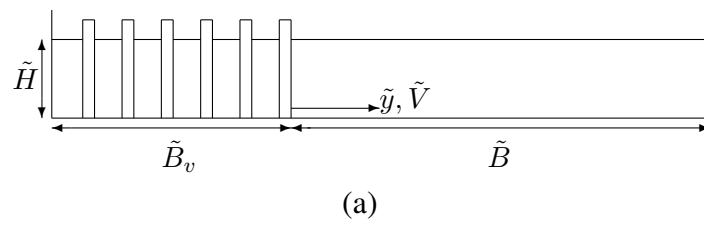


FIG. 1: Conceptual diagram of the channel with vegetation. (a) The cross-sectional view, and (b) the plan view.

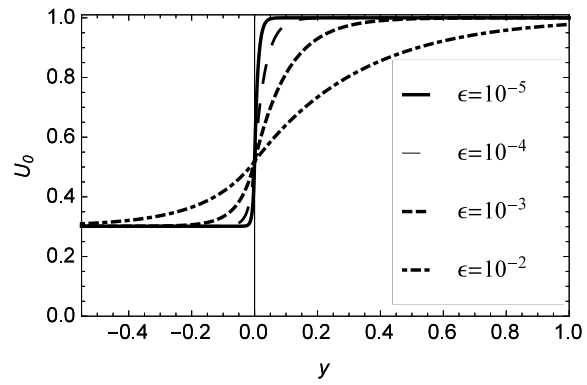


FIG. 2: Lateral distribution of the base flow velocity  $U_0$  for the case  $\beta = 0.05$ ,  $\alpha = 10$  and variable sub-depth eddy viscosity parameter  $\epsilon$ .

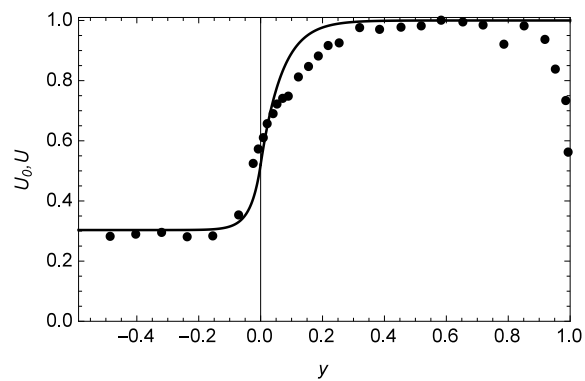
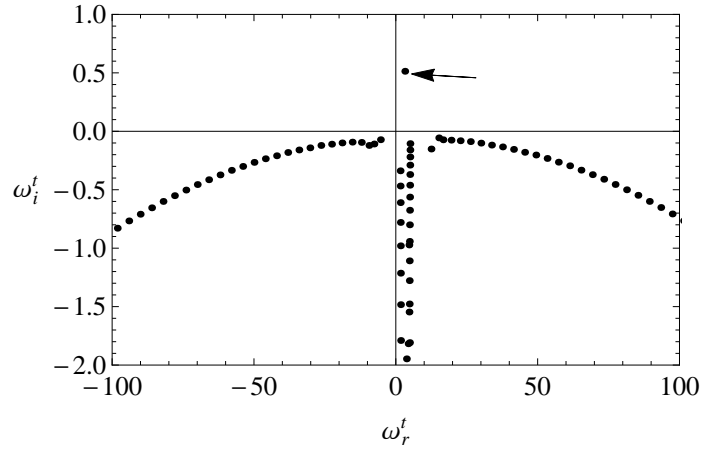
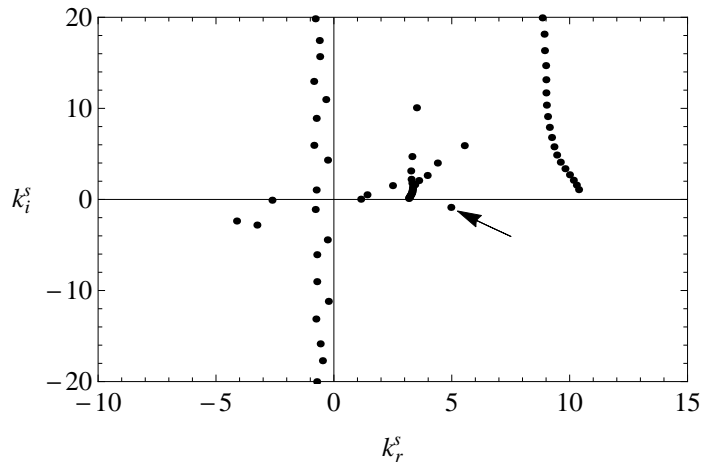


FIG. 3: Base state velocity  $U_0$  (continuous line) and measured streamwise velocity  $U$  at the developed state of perturbations along the lateral direction  $y$ , for run 1 of Ikeda et al. (1994), where  $\beta = 0.061$ ,  $\epsilon = 5.2 \times 10^{-4}$  and  $\alpha = 9.9$ .



(a)



(b)

FIG. 4: (a) Temporal spectrum for  $k^t = 5.0$  and (b) spatial spectrum for  $\omega^s = 3.2$ . The arrows indicate the eigenvalues to be selected for computing the perturbation growth.

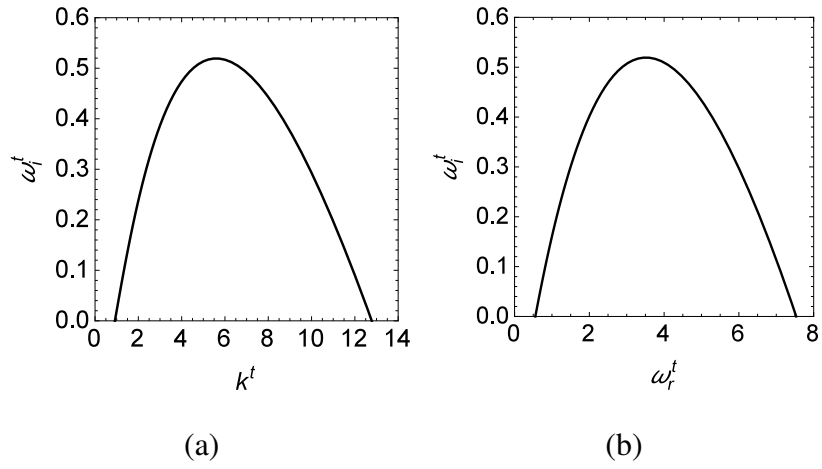


FIG. 5: Instability diagrams for the temporal case: (a)  $\omega_i^t$  versus  $k^t$ ; (b)  $\omega_i^t$  versus  $\omega_r^t$ .

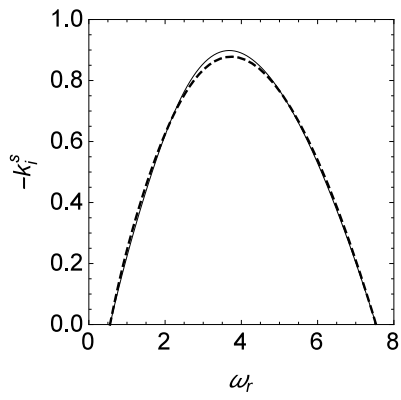


FIG. 6: Spatial growth rates  $-k_i^s$  obtained from the temporal analysis (dashed line) and the spatial analysis (continuous line).

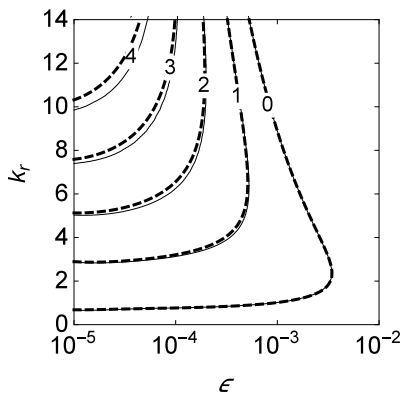


FIG. 7: Contours of the spatial growth rate  $-k_i^s$  determined from (a) the temporal analysis (dashed lines) and (b) the spatial analysis (continuous lines) in the  $\epsilon$ - $k_r$  plane.

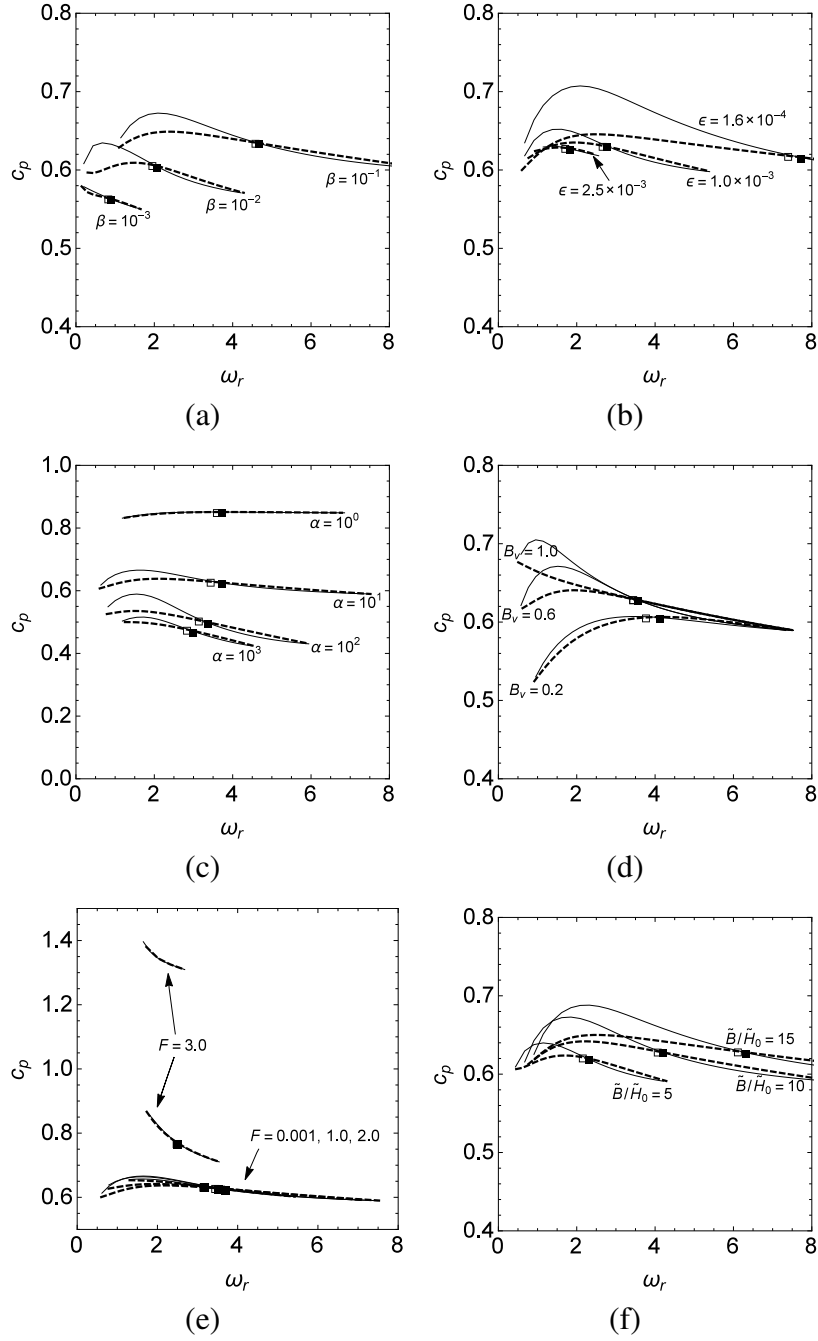


FIG. 8: Phase velocity  $c_p$  versus angular frequency  $\omega_r$  for the temporal analysis (dashed lines) and the spatial analysis (continuous lines). The phase velocity and angular frequency at the maximum amplification are indicated by  $\square$  for the temporal analysis and by  $\blacksquare$  for the spatial analysis.

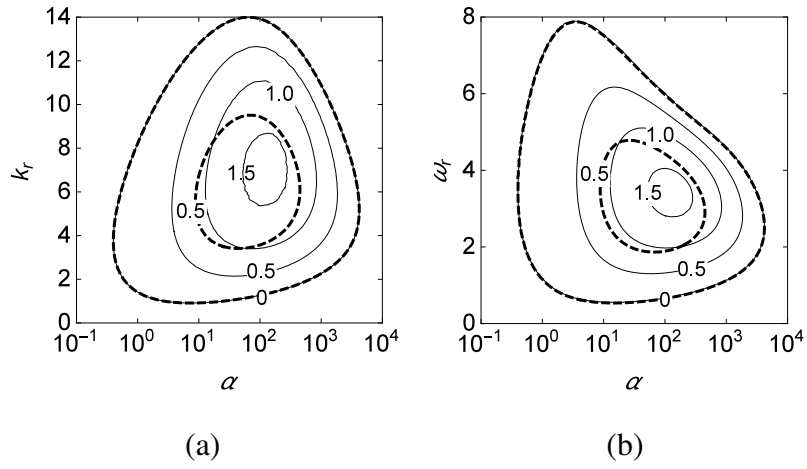


FIG. 9: Contours of  $\omega_i$  (dashed lines) and  $-k_i$  (continuous lines) in the (a)  $\alpha$ - $k_r$  plane and  $\alpha$ - $\omega_r$  plane.

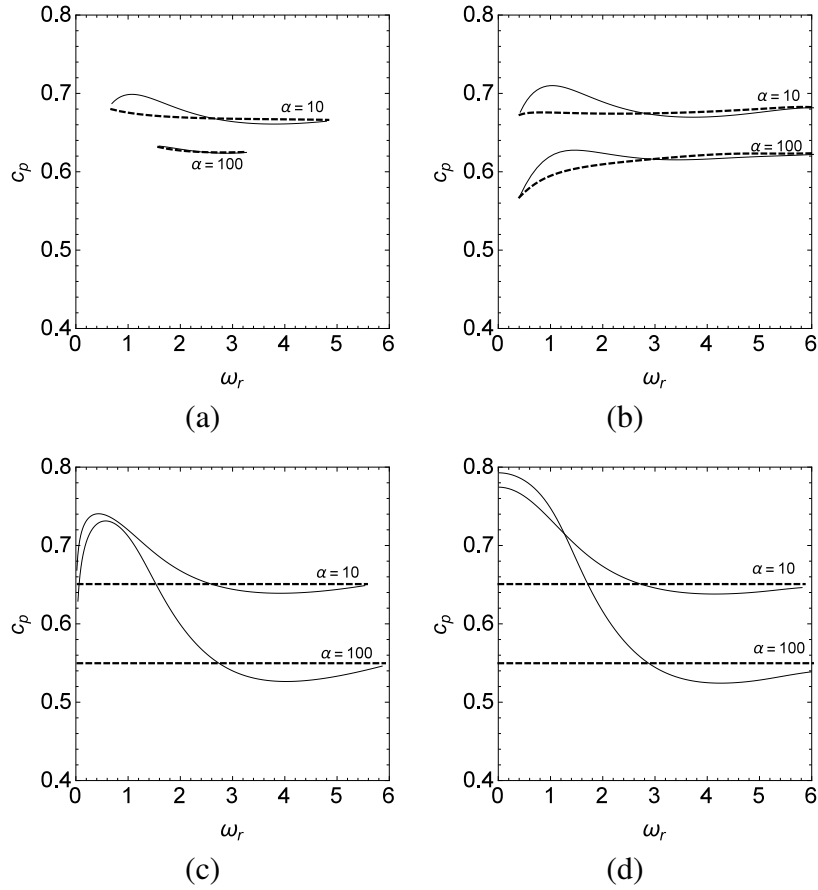


FIG. 10: Phase velocity  $c_p$  versus angular frequency  $\omega_r$  for the temporal analysis (dashed lines) and the spatial analysis (continuous lines) calculated using the base flow velocity of equation (32). (a) Perturbation equations (17–18) not modified; (b)  $\epsilon$  dropped from (17–18); (c)  $\beta$  dropped from (17–18); (d)  $\beta$  and  $\epsilon$  dropped from (17–18).

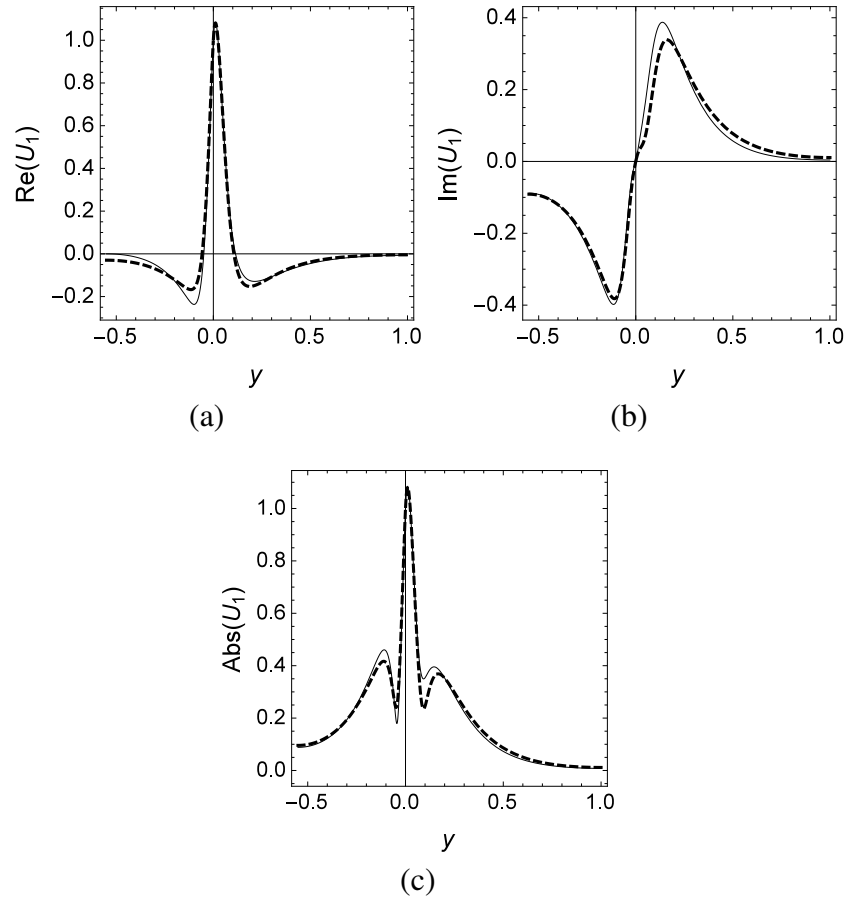


FIG. 11: Lateral distribution of the (a) real part, (b) imaginary part and (c) absolute value of eigenfunction  $U_1(y)$  at the maximum amplification in time (dashed curves) and space (continuous curves).